Research Article Vol. 9, No. 10 / October 2022 / Optica 1149

OPTICA

Simultaneous spectral recovery and CMOS micro-LED holography with an untrained deep neural network

Iksung Kang,[1,2,†] Marc de Cea,[1,†] Jin Xue,[1] Zheng Li,[1] George Barbastathis,[3,4,5] and Rajeev J. Ram[1,4,6]

[1]Department of Electrical Engineering and Computer Science, Massachusetts Institute of Technology, 77 Massachusetts Ave, Cambridge, Massachusetts 02139, USA
[2]Current address: University of California, Berkeley, California 94720, USA
[3]Department of Mechanical Engineering, Massachusetts Institute of Technology, 77 Massachusetts Ave, Cambridge, Massachusetts 02139, USA
[4]Singapore-MIT Alliance for Research and Technology (SMART) Centre, 1 Create Way, Singapore 117543, Singapore
[5]e-mail: gbarb@mit.edu
[6]e-mail: rajeev@mit.edu

Received 18 July 2022; revised 8 September 2022; accepted 8 September 2022; published 11 October 2022

Lensless holography promises compact, low-cost optical apparatus designs with similar performance to traditional imaging setups. Here, we propose the use of a silicon micro-LED fabricated in a commercial CMOS microelectronics process as the illumination source in a lensless holographic microscope. Its small emission area (<4 μm^2) ensures high spatial coherence without the need for a pinhole and results in a large NA setup, circumventing the limits to the source-to-sample distance encountered by conventional lensless holography apparatus. The scene is reconstructed using an untrained deep neural network architecture that simultaneously performs spectral recovery by learning from the given single experimental diffraction intensity. We envision this synergetic combination of CMOS micro-LEDs and the machine learning framework can be used in other computational imaging applications, such as a compact microscope for live-cell tracking or spectroscopic imaging of biological materials. © 2022 Optica Publishing Group under the terms of the Optica Open Access Publishing Agreement

https://doi.org/10.1364/OPTICA.470712

1. INTRODUCTION

Lensless imaging is a promising technique to realize low cost, high resolution, and large field-of- view (FoV) microscopes without requiring bulky and expensive optical components such as objectives and lenses [1]. It has been widely used in coherent diffraction imaging [2–7], ptychography [8–10], and phase tomography [11–14].

In lensless in-line holography, a (partially) spatially and temporally coherent light source illuminates the sample of interest, and a camera records the coherent interaction between the light scattered by the sample and the unscattered illumination light in the form of a hologram [15]. Computational backpropagation of the recorded hologram allows the recovery of the image at the sample plane [16,17] with a resolution usually limited by the pixel size and total area of the camera [18]. Recording multiple holograms at different positions both in the axial and transverse plane can improve the resolution to below a submicrometer level [19,20]. In-line holography microscopes have been employed for a variety of applications, including particle tracking [21], environmental monitoring [22], biological sample imaging [23], and metrology [24].

One of the main factors limiting the compactness and flexibility of lensless holographic microscopes is the requirement for spatial coherence. Usually, an LED is used as the illumination source, which requires the use of a pinhole to ensure a large enough degree of spatial coherence [25]. To reduce alignment tolerances and optical losses, big pinholes with diameters in the range of 20 -50 μm are used, resulting in a low NA for the illumination (NA $\approx 0.62\lambda/r$), which requires a source-to-sample separation on the order of 10 cm to ensure that the full FoV of the camera is illuminated. A further reduction in the form factor of lensless holographic microscopes could result in increased adoption of the this technique by enabling integration in portable devices and possibly even personal devices such as watches or phones. However, this change requires rethinking the illumination source and shift from the ubiquitous LED + pinhole configuration.

Lensless holography requires computational backpropagation to retrieve an image at the sample plane. Traditional reconstruction methods require detailed knowledge of the experimental setup for accurate reconstruction and are sensitive to nonidealities such as optical aberrations, the presence of noise, and the twin image problem. Deep neural network architectures have been widely used to improve the quality of image reconstruction and have been shown to be robust to such nonidealities [5,7,26–29]. Of

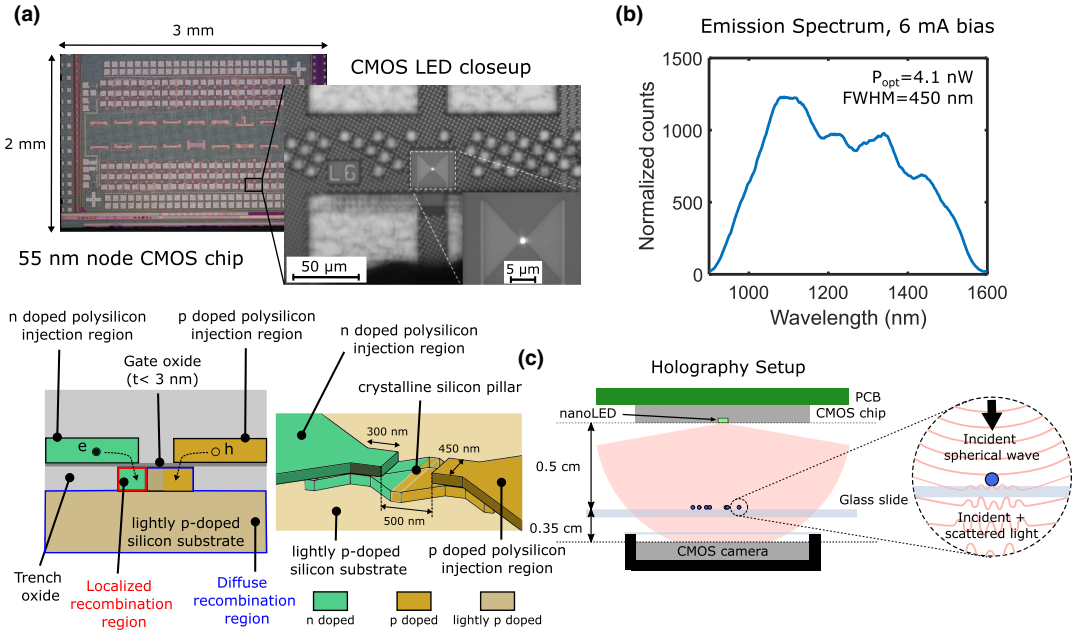

Fig. 1. CMOS LED light source and holography apparatus. (a) On the top, a micrograph of the 2 mm × 3 mm 55 nm bulk CMOS chip is shown, as well as a closeup of the tapered LED source. The inset shows the light emission spot when the LED is forward biased, demonstrating an emission spot below 1.3 µm × 1.3 µm. On the bottom, a schematic of the LED configuration is shown. 10 µm long tapers in the polysilicon layer are used to inject carriers into a crystalline silicon pillar region via breakdown of the thin gate oxide. Once in the crystalline silicon, phonon-assisted carrier recombination results in light emission. (b) The experimentally measured emission spectrum when the LED source is biased at a current of 6 mA. The spectrum has an FWHM of 450 nm with a peak wavelength around 1100 nm. (c) Schematic of the lensless holography microscope. The light emitted by the CMOS LED illuminates the sample, and the coherent interaction between the light that interacts with the sample and the unscattered light is recorded by a CMOS camera in the form of a hologram. The small emission spot of the CMOS LED eliminates the need for a pinhole, and its large numerical aperture allows for placement of the source very close to the sample, resulting in a compact setup.

particular importance here is how to deal with broadband illumination sources: If the illumination source has a finite spectral bandwidth, the assumption of monochromatic illumination typical of traditional reconstruction techniques limits the achievable resolution. In [30,31], a modification of monochromatic iterative phase retrieval using a priori known source spectrum was introduced for applications in X-ray imaging. Additionally, broadband diffraction models to generate object-diffraction pairs have been used in end-to-end deep neural networks for object retrieval [32]. For these implementations, however, access to the prior knowledge of the source spectrum is of concern, which requires an extra step for spectral measurements with an optical spectrum analyzer or spectroscopy.

In this work, we present what we believe, to the best of our knowledge, is a novel lensless holographic microscope incorporating advancements in both the hardware and the computational reconstruction algorithm to address the aforementioned issues.

The untrained reconstruction demonstrated here allows us to use novel light sources without prior knowledge of the source spectrum or beam profile. We employ, what we believe, to the best of our knowledge, is a novel silicon micro-LED fabricated in a fully commercial, unmodified bulk CMOS microelectronics process (GlobalFoundries 55BCDL). While silicon is usually not regarded as a good light emitter due to its indirect bandgap, its efficiency is set by the competition between radiative and nonradiative processes (surface and Shockley–Read–Hall recombination). Our LED design, shown in Fig. 1(a), minimizes nonradiative recombination by taking advantage of the high-quality surface passivation of the crystalline silicon with the native oxide. The surface recombination velocity can be three to four orders of magnitude lower than in III–V materials typically used for the realization of LEDs. Our spectrally broadband LED uses a vertical n–p junction in crystalline silicon that is formed between an n-doped pillar and the p-doped substrate, similar to [33] scaled to submicrometer dimensions. Doped polysilicon tapers [the orange and green shapes in Fig. 1(a)] are used to inject the carriers into the crystalline silicon through the breakdown of the <3 nm thick gate oxide [34]. Because these are homojunction devices, recombination occurs in both the n region (which is 500 nm × 500 nm) and the p substrate, where recombination is diffuse. The spatially localized recombination in the n region provides spatially coherent, but spectrally broad, illumination for digital holography. These nanoscale devices are operated at high current density [MA/cm^2], which results in additional radiation from the submicron p-contact regions due to impact ionization [35]. The combination of spatially confined LED emission and submicron thermal emission gives rise to a very broad spectral bandwidth with sufficient spatial coherence for use as a holographic light source.

2. METHODS

As shown in Fig. 1(a), light emission is confined to the crystalline silicon island and its emission area is around 1.3 µm × 1.3 µm. The spectrum of the emitted light measured with a diffractive spectrometer using an InGaAs camera is shown in Fig. 1(b), revealing a peak wavelength of 1.1 µm (close to the bandgap of silicon) and a 3 dB spectral bandwidth of about 450 nm. Such a large optical

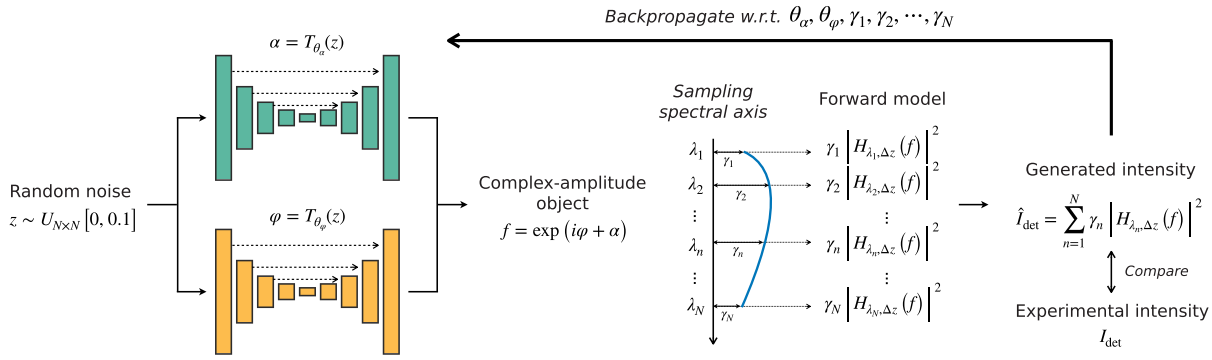

Fig. 2. Untrained deep neural network framework for simultaneous spectral and holographic reconstruction. Two untrained deep neural networks were used: one for phase and one for amplitude, and then we backpropagate for the network weights θ_α, θ_φ, as well as the learned spectrum γ_n $(n = 1, 2, \cdots, N)$.

bandwidth results in a lower temporal coherence compared to typical commercial LEDs that have spectral bandwidths below 20 nm. This motivates the use of the spectroscopic image reconstruction framework as presented below.

A schematic of the experimental apparatus is shown in Fig. 1(c). The small emission area of our CMOS LED source ensures reasonable spatial coherence without a pinhole, as well as a large NA that allows the source-to-sample distance to be greatly decreased below 5 mm while maintaining a large FoV. This results in a very compact system with a total source-to-camera distance below 1 cm. We use a ZWO ASI1600MM CMOS camera with a pixel pitch of 3.8 μm and a total imaging area of 17.7 × 13.4 mm.

On the reconstruction algorithm side, the complex amplitude of objects is expressed with two separate deep neural networks (one for amplitude and one for phase), and the source spectrum is learned from a given experimental diffraction intensity. We use an untrained approach called deep image prior (DIP) for the deep neural network implementation [36]. DIP works as an alternative, highly nonlinear representation of multidimensional objects with a uniformly sampled random input noise, parameterized with neural network weights. DIP has been applied to denoising [36–38], phase retrieval [27,39], holography [40], Fourier ptychography [41], and tomographic imaging [42–45], whose implementation is similar to implicit neural representation that represents an object onto input coordinates as a continuous function [46–48]. Our computational framework also accounts for the nonmonochromaticity of the illumination and can learn the relative contributions of each wavelength to the recorded hologram without any previous knowledge of the spectrum. In essence, our algorithm can estimate the optical spectrum of the illumination, which is demonstrated to be comparable to the experimentally measured source spectrum and improves the quality of the reconstructed image. Finally, we adopt total variation regularization to suppress fringe pattern artifacts often entailed with inversion from diffraction intensities due to its ill-posed nature.

Figure 2 visualizes the training procedure of the proposed algorithm. Uniformly sampled random noise z is the input to two DIP architectures representing absorption and phase delay profiles of the object of interest. The architectures are parametrized by θ_α and θ_φ, respectively. A sigmoid activation function is applied at the end of the architectures to make the absorption profile α range between $[\alpha_{\min}, \alpha_{\max}](= [0.0, 1.0])$ and the phase profile φ between $[\varphi_{\min}, \varphi_{\max}]$. Together, they define the complex-amplitude object $f = \exp(i\varphi + \alpha)$, gradually updated throughout training. To account for the spectral shape of the illumination, we uniformly sample the wavelength axis with N points (i.e., $\lambda_1, \lambda_2, \cdots, \lambda_N$), and define forward operators for each wavelength. Here, we use a nonparaxial free-space propagation kernel [49] to describe the diffraction of the optical wavefield from the object when propagating the sample-camera distance Δz in free space along the propagation direction

$$\begin{aligned} &H_{\lambda_n,\Delta z}(f) \\ &= \mathcal{F}^{-1}\left[\mathcal{F}[f] \circ \exp\left(-i\Delta z\left(k_n - \mathrm{Re}\left[\sqrt{k_n^2 - k_x^2 - k_y^2}\right]\right)\right)\right], \\ &k_n = \frac{2\pi}{\lambda_n}. \end{aligned} \tag{1}$$

Parameters γ_n $(n = 1, 2, \cdots, N)$ account for the unequal contribution of each wavelength λ_n to the experimental diffraction intensity I_{det}:

$$\hat{I}_{\text{det}} = \sum_{n=1}^{N} \gamma_n \left| H_{\lambda_n,\Delta z}(f) \right|^2. \tag{2}$$

Now, the inverse problem is reduced to finding joint solutions α and φ that make $\hat{I}_{\text{det}}$ as close as possible to I_{det} and to simultaneously optimize the underlying imaging physics represented with λ_n's. To solve the inverse problem, we use the Adam optimizer [50] and minimize the loss function defined as

$$\begin{aligned} &\mathcal{L}(\hat{I}_{\text{det}}, I_{\text{det}}; \theta_\alpha, \theta_\varphi, \gamma_1, \gamma_2, \cdots, \gamma_N) \\ &= \mathrm{MSE}\left(\hat{I}_{\text{det}}, I_{\text{det}}\right) + \kappa_1 \mathrm{NPCC}\left(\hat{I}_{\text{det}}, I_{\text{det}}\right) + \kappa_2\left(1 - \sum_{n=1}^{N}\gamma_n\right) \\ &\quad + \kappa_3 \sum_{n=1}^{N} \mathrm{ReLU}(-\gamma_n) + \kappa_4(\mathrm{TV}(\alpha) + \mathrm{TV}(\varphi)), \end{aligned} \tag{3}$$

where MSE stands for mean-squared error, NPCC for negative Pearson correlation coefficient, and TV for total variation. The mean-squared error term has been a standard for training DIP architectures [36,38], originating from the derivation of a maximum a posteriori (MAP) estimate with the assumption of

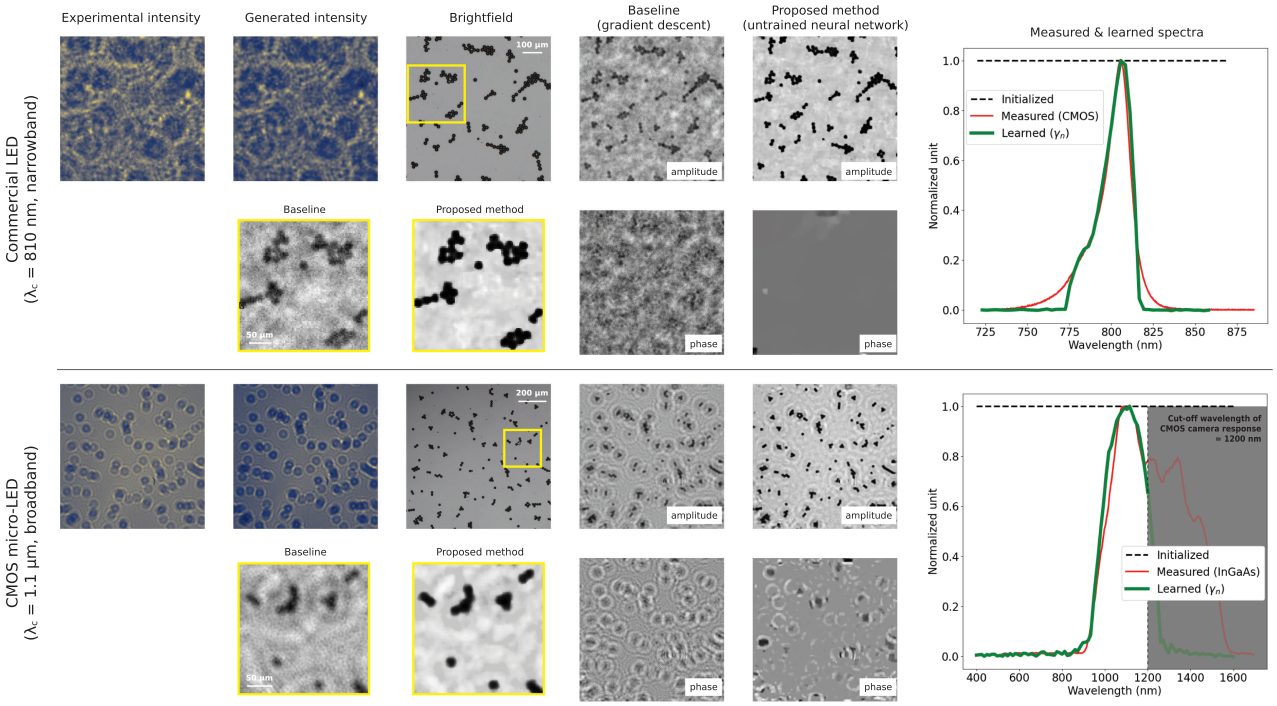

Fig. 3. Qualitative comparison in 20- µm bead reconstructions of a baseline method and the proposed architecture for a narrowband commercial LED (top) and broadband CMOS LED (bottom). Quantitatively, the Pearson correlation coefficient was used as a metric to compare the reconstructions with the brightfield image as the ground truth (see Supplement 1, Fig. S2). Experimentally measured and learned spectra for both illumination sources are also compared.

Gaussian noise on a measurement. Equation (3) also includes three regularization terms with regularization weights fixed as $\kappa_1, \kappa_2 = 10,\ \kappa_3 = 0.25$ with a tunable κ_4. The first regularizer is the NPCC, which has been proven to stabilize the training process and achieve higher reconstruction fidelity in phase retrieval applications with convolutional neural networks [26,51]. Similarly, we also observe this in the current study as well as speeding up retrieval of γ_n's. The second regularizer is essentially a Lagrange multiplier imposing the constraint on γ_n's to be normalized with their sum being 1 and non-negative. Finally, TV is applied to both the absorption and phase delay profiles of the object f to smooth out the fringe pattern artifacts. TV regularization weight and Δz are image-specific, and the details in these hyperparameters can be found in Supplement 1, Table S1. The optimization process takes between 400 and 600 epochs for convergence, with a total computation time below 10 minutes. For more details, see Supplement 1, Table S2. All optimization procedures are performed on the MIT Supercloud [52] with Intel Xeon Gold 6248 and NVIDIA Volta V100 GPU with 32 GB VRAM.

3. RESULTS

We first demonstrate that the proposed untrained deep neural network framework works for different illumination sources with different characteristics. To do so, we compare the reconstructions of a baseline method and the proposed deep image prior architecture under the illumination of a narrowband commercial LED ($\lambda_c = 810$ nm, bandwidth $\simeq$50 nm) and the broadband CMOS micro-LED presented in this work ($\lambda_c = 1.1$ µm, bandwidth $\simeq$450 nm), as shown in Fig. 3.

A steepest gradient descent algorithm is considered as the baseline method, and the complex-amplitude object $f = \exp(i\varphi + \alpha)$ is retrieved by solving the optimization problem

$$\hat{f}_{\text{baseline}} = \text{argmin}_f \left[\frac{1}{2} \left| \sum_{n=1}^{N} \xi_n \left| H_{\lambda_n, \Delta z}(f) \right|^2 - I_{\text{det}} \right|^2 \right], \quad (4)$$

where I_{det} is the experimental diffraction intensity and ξ_n $(n = 1, 2, \cdots, N)$ is fixed to the measured spectrum of either the commercial LED or our CMOS LED.

The proposed model reconstructions presented in Figs. 3 and 4 are generated with γ_n $(n = 1, 2, \cdots, N)$ in Eq. (3) initialized as a uniform distribution with $N = 50$ (commerical LED) and $N = 100$ (CMOS LED) samples. A larger number of samples (N) is considered for the CMOS LED to cover its much broader spectrum. More details are presented in Supplement 1, Fig. S1.

Figure 3 compares the resulting reconstructions of the baseline and proposed methods, showing better contrast and a background with fewer artifacts when we employ our untrained deep neural network framework. Here, the total variation effectively suppresses fringe pattern artifacts existing around the beads, resulting in reconstructions with improved contrast. Table S2 in Supplement 1 shows a quantitative comparison between the baseline and our proposed method. Figure 3 also shows the illumination spectrum learned with our algorithm and compares it to the real spectrum measured experimentally with a spectrometer. The learned γ_n's of both sources are in close agreement to its experimentally measured spectra up to 1200 nm, equivalent to a blind spectroscopic analysis solely based on an experimental diffraction intensity. The proposed method achieves a Pearson correlation coefficient of 0.9838 (commercial LED) and 0.9831 (CMOS LED) in blind recovery of the

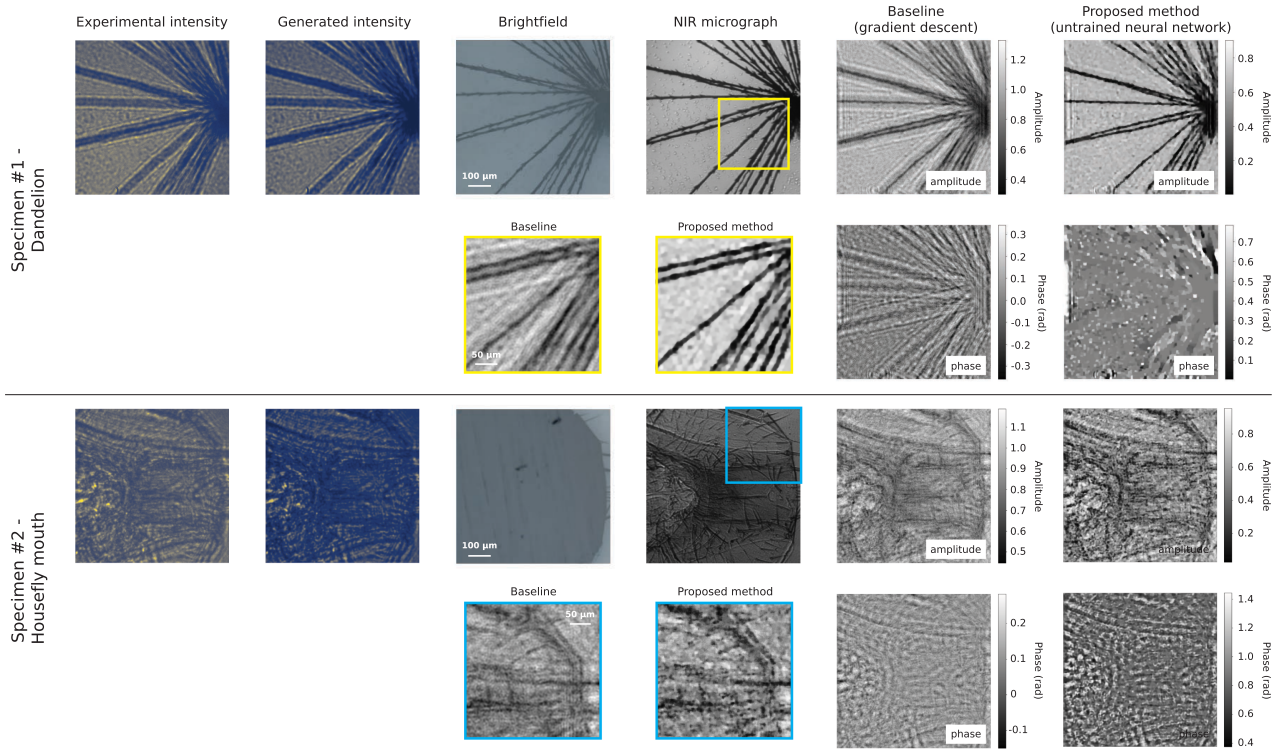

Fig. 4. Qualitative comparison between brightfield image, NIR micrographs, and complex object reconstructions by the proposed untrained deep neural network framework under our CMOS micro-LED illumination across different biological specimens.

sources up to 1200 nm. Considering our ZWO CMOS camera's responsivity falls off to nearly zero above 1200 nm, as shown in Supplement 1, Fig. S3, we should not expect spectral recovery above the cutoff wavelength.

We further demonstrate the performance of the proposed framework with different types of biological specimens, and the reconstructions are shown in Fig. 4. Under the illumination of our CMOS LED at a near-IR region, the dandelion and housefly mouth specimens are mostly absorptive. The proposed model can resolve object features with better contrast in either amplitude or phase, thus better matching the corresponding brightfield image and NIR micrograph.

Hyperparameters fixed and initialized in Eq. (3) for imaging these biological specimens are presented in Supplement 1, Table S1. We note that the TV regularization parameter κ_4 must be carefully chosen. Objects with more complicated features require a much smaller κ_4 compared to objects with simpler features to avoid oversmoothing. We also note that the computational reconstruction distances listed in Supplement 1, Table S1, are significantly larger than the physical-sample-to-camera distance in the experimental setup. This is because the LED source generates a distorted spherical wave but the reconstruction algorithm assumes plane wave illumination, an approach that simplifies the computation and does not decrease the reconstruction quality, but requires rescaling the reconstruction distance: $d_{\text{sample_camera-recon}} = d^2_{\text{source_camera-setup}}/d_{\text{sample_camera-setup}}$ [17], as shown in Table S1 in Supplement 1.

4. DISCUSSION

In conclusion, we have presented a lensless holography setup that employs what we believe, to the best of our knowledge, is a novel silicon LED realized in an unmodified commercial CMOS process as the illumination source. Its small emission area eliminates the need for a pinhole and its large NA allows the source-to-camera distance to be reduced to below 1 cm, resulting in a highly compact microscope. We also employ a new, untrained deep neural network framework that accounts for the broad spectral bandwidth of the source and that includes total variation regularization for improved contrast. Although the method is iterative and requires a few minutes to get estimates, it saves time for data preparation as paired datasets are not required for training. It also provides blind source spectrum recovery from a single diffracted intensity pattern at the same time as holographic image reconstruction, which makes a complete departure from any existing supervised learning approaches.

Improvements to the obtained resolution can be achieved by subpixel sampling techniques using an array of our CMOS LEDs, similar to [53]. It is worth noting that we can leverage the low cost and scalability of the microelectronics CMOS processes to implement such an array without increasing the system complexity, cost, or form factor. Furthermore, control electronics (and possible even the imager) could be integrated in the same chip as the illumination by exploiting the available electronics in the process. On the computational side, approaches to increase resolution under low light conditions, such as in [5,7,26], could be used to increase the image quality. We believe this combination of broadband CMOS LEDs with optical spectrum-aware machine learning frameworks could enable applications such as spectroscopic imaging of biological materials and new metrology techniques.

Funding. Intelligence Advanced Research Projects Activity (FA8650-17-C-9113); National Research Foundation Singapore; Korea Foundation for Advanced Studies.

Acknowledgment. Authors Iksung Kang and George Barbastathis acknowledge funding from Intelligence Advanced Research Projects Activity and acknowledge the MIT SuperCloud and Lincoln Laboratory Supercomputing Center for providing (HPC, database, consultation) resources that have contributed to the research results reported within this paper. Author Iksung Kang acknowledges support from Korea Foundation for Advanced Studies (KFAS). This research was supported by the National Research Foundation (NRF), Prime Minister's Office, Singapore under its Campus for Research Excellence and Technological Enterprise (CREATE) program. Disruptive Sustainable Technology for Agricultural Precision (DiSTAP) and Critical Analytics for Manufacturing Personalized-Medicine (CAMP) are interdisciplinary research groups (IRG) of the Singapore MIT Alliance for Research and Technology (SMART) Centre.

Disclosures. The authors declare no competing interests.

Data availability. Code should be publicly available at [54].

Supplemental document. See Supplement 1 for supporting content.

[†]These authors contributed equally to this work.

REFERENCES

1. V. Boominathan, J. T. Robinson, L. Waller, and A. Veeraraghavan, "Recent advances in lensless imaging," Optica **9**, 1–16 (2022).
2. D. J. Brady, K. Choi, D. L. Marks, R. Horisaki, and S. Lim, "Compressive holography," Opt. Express **17**, 13040–13049 (2009).
3. H. N. Chapman and K. A. Nugent, "Coherent lensless X-ray imaging," Nat. Photonics **4**, 833–839 (2010).
4. A. Sinha, J. Lee, S. Li, and G. Barbastathis, "Lensless computational imaging through deep learning," Optica **4**, 1117–1125 (2017).
5. I. Kang, F. Zhang, and G. Barbastathis, "Phase extraction neural network (PhENN) with coherent modulation imaging (CMI) for phase retrieval at low photon counts," Opt. Express **28**, 21578–21600 (2020).
6. L. Waller, L. Tian, and G. Barbastathis, "Transport of intensity phase-amplitude imaging with higher order intensity derivatives," Opt. Express **18**, 12552–12561 (2010).
7. M. Deng, S. Li, A. Goy, I. Kang, and G. Barbastathis, "Learning to synthesize: robust phase retrieval at low photon counts," Light Sci. Appl. **9**, 36 (2020).
8. A. M. Maiden and J. M. Rodenburg, "An improved ptychographical phase retrieval algorithm for diffractive imaging," Ultramicroscopy **109**, 1256–1262 (2009).
9. M. Holler, A. Diaz, M. Guizar-Sicairos, P. Karvinen, E. Färm, E. Härkönen, M. Ritala, A. Menzel, J. Raabe, and O. Bunk, "X-ray ptychographic computed tomography at 16 nm isotropic 3D resolution," Sci. Rep. **4**, 3857 (2014).
10. J. M. Rodenburg and H. M. Faulkner, "A phase retrieval algorithm for shifting illumination," Appl. Phys. Lett. **85**, 4795–4797 (2004).
11. A. Goy, G. Rughoobur, S. Li, K. Arthur, A. I. Akinwande, and G. Barbastathis, "High-resolution limited-angle phase tomography of dense layered objects using deep neural networks," Proc. Natl. Acad. Sci. USA **116**, 19848–19856 (2019).
12. M. Guizar-Sicairos, A. Diaz, M. Holler, M. S. Lucas, A. Menzel, R. A. Wepf, and O. Bunk, "Phase tomography from X-ray coherent diffractive imaging projections," Opt. Express **19**, 21345–21357 (2011).
13. I. Kang, A. Goy, and G. Barbastathis, "Dynamical machine learning volumetric reconstruction of objects' interiors from limited angular views," Light Sci. Appl. **10**, 74 (2021).
14. M. Holler, M. Guizar-Sicairos, E. H. Tsai, R. Dinapoli, E. Müller, O. Bunk, J. Raabe, and G. Aeppli, "High-resolution non-destructive three-dimensional imaging of integrated circuits," Nature **543**, 402–406 (2017).
15. D. Gabor, "A new microscopic principle," Nature **161**, 777–778 (1948).
16. W. Xu, M. H. Jericho, I. A. Meinertzhagen, and H. J. Kreuzer, "Digital in-line holography of microspheres," Appl. Opt. **41**, 5367–5375 (2002).
17. T. Latychevskaia and H.-W. Fink, "Practical algorithms for simulation and reconstruction of digital in-line holograms," Appl. Opt. **54**, 2424–2434 (2015).
18. D. P. Kelly, B. M. Hennelly, N. Pandey, T. J. Naughton, and W. T. Rhodes, "Resolution limits in practical digital holographic systems," Opt. Eng. **48**, 095801 (2009).
19. W. Bishara, U. Sikora, O. Mudanyali, T.-W. Su, O. Yaglidere, S. Luckhart, and A. Ozcan, "Holographic pixel super-resolution in portable lensless on-chip microscopy using a fiber-optic array," Lab Chip **11**, 1276–1279 (2011).
20. A. Greenbaum, U. Sikora, and A. Ozcan, "Field-portable wide-field microscopy of dense samples using multi-height pixel super-resolution based lensfree imaging," Lab Chip **12**, 1242–1245 (2012).
21. P. Memmolo, L. Miccio, M. Paturzo, G. D. Caprio, G. Coppola, P. A. Netti, and P. Ferraro, "Recent advances in holographic 3D particle tracking," Adv. Opt. Photon. **7**, 713–755 (2015).
22. Y. Wu and A. Ozcan, "Lensless digital holographic microscopy and its applications in biomedicine and environmental monitoring," Methods **136**, 4–16 (2018), Special issues in methods in quantitative phase imaging in life science.
23. Y. Wu, Y. Zhang, W. Luo, and A. Ozcan, "Demosaiced pixel super-resolution for multiplexed holographic color imaging," Sci. Rep. **6**, 28601 (2016).
24. T. Kreis, "Application of digital holography for nondestructive testing and metrology: a review," IEEE Trans. Ind. Inf. **12**, 240–247 (2016).
25. Y. Deng and D. Chu, "Coherence properties of different light sources and their effect on the image sharpness and speckle of holographic displays," Sci. Rep. **7**, 5893 (2017).
26. A. Goy, K. Arthur, S. Li, and G. Barbastathis, "Low photon count phase retrieval using deep learning," Phys. Rev. Lett. **121**, 243902 (2018).
27. F. Wang, Y. Bian, H. Wang, M. Lyu, G. Pedrini, W. Osten, G. Barbastathis, and G. Situ, "Phase imaging with an untrained neural network," Light Sci. Appl. **9**, 77 (2020).
28. Y. Rivenson, Y. Zhang, H. Günaydn, D. Teng, and A. Ozcan, "Phase recovery and holographic image reconstruction using deep learning in neural networks," Light Sci. Appl. **7**, 17141 (2018).
29. Y. Rivenson, Y. Wu, and A. Ozcan, "Deep learning in holography and coherent imaging," Light Sci. Appl. **8**, 85 (2019).
30. J. Huijts, S. Fernandez, D. Gauthier, M. Kholodtsova, A. Maghraoui, K. Medjoubi, A. Somogyi, W. Boutu, and H. Merdji, "Broadband coherent diffractive imaging," Nat. Photonics **14**, 618–622 (2020).
31. B. Abbey, L. W. Whitehead, H. M. Quiney, D. J. Vine, G. A. Cadenazzi, C. A. Henderson, K. A. Nugent, E. Balaur, C. T. Putkunz, A. G. Peele, G. J. Williams, and I. McNulty, "Lensless imaging using broadband X-ray sources," Nat. Photonics **5**, 420–424 (2011).
32. J. Wu, L. Cao, and G. Barbastathis, "DNN-FZA camera: a deep learning approach toward broadband FZA lensless imaging," Opt. Lett. **46**, 130–133 (2021).
33. J. Xue, J. Kim, A. Mestre, K. M. Tan, D. Chong, S. Roy, H. Nong, K. Y. Lim, D. Gray, D. Kramnik, A. Atabaki, E. Quek, and R. J. Ram, "Low voltage, high brightness CMOS leds," in *IEEE International Electron Devices Meeting (IEDM)* (2020), pp. 33.5.1–33.5.4.
34. N. Akil, V. E. Houtsma, P. LeMinh, J. Holleman, V. Zieren, D. de Mooij, P. H. Woerlee, A. van den Berg, and H. Wallinga, "Modeling of light-emission spectra measured on silicon nanometer-scale diode antifuses," J. Appl. Phys. **88**, 1916–1922 (2000).
35. M. Rasras, I. De Wolf, G. Groeseneken, R. Degraeve, and H. Maes, "Substrate hole current origin after oxide breakdown," in *International Electron Devices Meeting (IEDM)*, Technical digest (2000), pp. 537–540.
36. D. Ulyanov, A. Vedaldi, and V. Lempitsky, "Deep image prior," in *Proceedings of the IEEE/CVF Conference on Computer Vision and Pattern Recognition (CVPR)* (2018), pp. 9446–9454.
37. G. Mataev, P. Milanfar, and M. Elad, "Deep RED: deep image prior powered by RED," in *Proceedings of the IEEE/CVF International Conference on Computer Vision Workshops (ICCVW)* (2019).
38. J. Liu, Y. Sun, X. Xu, and U. S. Kamilov, "Image restoration using total variation regularized deep image prior," in *ICASSP 2019-2019 IEEE International Conference on Acoustics, Speech and Signal Processing (ICASSP)* (IEEE, 2019), pp. 7715–7719.
39. E. Bostan, R. Heckel, M. Chen, M. Kellman, and L. Waller, "Deep phase decoder: self-calibrating phase microscopy with an untrained deep neural network," Optica **7**, 559–562 (2020).
40. C. Bai, T. Peng, J. Min, R. Li, Y. Zhou, and B. Yao, "Dual-wavelength in-line digital holography with untrained deep neural networks," Photon. Res. **9**, 2501–2510 (2021).
41. L. Boominathan, M. Maniparambil, H. Gupta, R. Baburajan, and K. Mitra, "Phase retrieval for Fourier ptychography under varying amount of measurements," arXiv:1805.03593 (2018).

42. Z. Wu, Y. Sun, A. Matlock, J. Liu, L. Tian, and U. S. Kamilov, "SIMBA: Scalable inversion in optical tomography using deep denoising priors," IEEE J. Sel. Top. Signal Process. **14**, 1163–1175 (2020).
43. D. O. Baguer, J. Leuschner, and M. Schmidt, "Computed tomography reconstruction using deep image prior and learned reconstruction methods," Inverse Probl. **36**, 094004 (2020).
44. K. C. Zhou and R. Horstmeyer, "Diffraction tomography with a deep image prior," Opt. Express **28**, 12872–12896 (2020).
45. K. Gong, C. Catana, J. Qi, and Q. Li, "PET image reconstruction using deep image prior," IEEE Trans. Med. Imaging **38**, 1655–1665 (2018).
46. V. Sitzmann, J. Martel, A. Bergman, D. Lindell, and G. Wetzstein, "Implicit neural representations with periodic activation functions," in *Advances in Neural Information Processing Systems 33*, (2020) pp. 7462–7473.
47. Y. Sun, J. Liu, M. Xie, B. Wohlberg, and U. S. Kamilov, "Coil: coordinate-based internal learning for tomographic imaging," IEEE Trans. Comput. Imaging **7**, 1400–1412 (2021).
48. Y. Chen, S. Liu, and X. Wang, "Learning continuous image representation with local implicit image function," in *Proceedings of the IEEE/CVF Conference on Computer Vision and Pattern Recognition (CVPR)* (2021), pp. 8628–8638.
49. M. D. Feit and J. A. Fleck, "Beam nonparaxiality, filament formation, and beam breakup in the self-focusing of optical beams," J. Opt. Soc. Am. B **5**, 633–640 (1988).
50. D. P. Kingma and J. Ba, "Adam: a method for stochastic optimization," arXiv:1412.6980 (2014).
51. S. Li, M. Deng, J. Lee, A. Sinha, and G. Barbastathis, "Imaging through glass diffusers using densely connected convolutional networks," Optica **5**, 803–813 (2018).
52. A. Reuther, J. Kepner, C. Byun, S. Samsi, W. Arcand, D. Bestor, B. Bergeron, V. Gadepally, M. Houle, M. Hubbell, M. Jones, A. Klein, L. Milechin, J. Mullen, A. Prout, A. Rosa, C. Yee, and P. Michaleas, "Interactive supercomputing on 40,000 cores for machine learning and data analysis," in *IEEE High Performance extreme Computing Conference (HPEC)* (IEEE, 2018), pp. 1–6.
53. E. Prajapati, S. Kumar, and S. Kumar, "Muscope: a miniature on-chip lensless microscope," Lab Chip **21**, 4357–4363 (2021).
54. I. Kang, "Code for 'Simultaneous spectral recovery and CMOS micro-LED holography with an untrained deep neural network'," Github (2022), https://github.com/iksungk/simultaneous_recovery.